

Radio Science

RESEARCH ARTICLE

10.1029/2019RS006869

Special Section:

RADIO CHANNEL MODELLING
 FOR 5G MILLIMETRE WAVE
 COMMUNICATIONS IN BUILT
 ENVIRONMENTS

Key Points:

- Nonspecular scattering from buildings is shown to be a key factor for path-loss determination, and not only for wideband characteristics
- Scattering from large objects such as cars is also very important for RF coverage in NLOS locations
- The work's aim is to analyze mm-wave urban propagation and to tune a ray-tracing model for realistic prediction in the same environment

Correspondence to:

E. M. Vitucci,
 enricomaria.vitucci@unibo.it

Citation:

Vitucci, E. M., Degli-Esposti, V., Mani, F., Fuschini, F., Barbiroli, M., Gan, M., et al. (2019). Tuning ray tracing for mm-wave coverage prediction in outdoor urban scenarios. *Radio Science*, 54, 1112–1128. <https://doi.org/10.1029/2019RS006869>

Received 30 APR 2019






Accepted 24 OCT 2019

Accepted article online 9 NOV 2019

Published online 25 NOV 2019

©2019. American Geophysical Union.
 All Rights Reserved.

Tuning Ray Tracing for Mm-wave Coverage Prediction in Outdoor Urban Scenarios

Enrico M. Vitucci¹ , Vittorio Degli-Esposti¹ , Francesco Mani^{1,2} , Franco Fuschini¹ , Marina Barbiroli¹ , Mingming Gan³, Chao Li³, Jianyao Zhao³, and Zhimeng Zhong³

¹Dipartimento di Ingegneria dell'Energia Elettrica e dell'Informazione "G. Marconi", University of Bologna, Bologna, Italy, ²Eurecom, Sophia Antipolis, France, ³Propagation and Simulation Technology Lab, Huawei Technologies Co., Ltd., Shanghai, China

Abstract Propagation characteristics at 26, 28, and 38 GHz (Ka band) in outdoor environments are analyzed through path loss measurements in two different urban scenarios and used to tune a ray-tracing model, with specific focus on nonspecular scattering and vegetation attenuation.

The contribution from nonspecular components in non-line-of-sight conditions is shown to be much more important than expected even for narrowband prediction, differently to what was found in previous studies at lower frequencies. Attenuation through vegetation is also very important and can be described using vegetation polygons and a simple linear attenuation model. When these effects are modeled inside the ray-tracing tool, prediction accuracy is good. However, scattering from vehicles and other cluttering objects is shown to give a relevant contribution in deep non-line-of-sight locations, and further work is needed to systematically model such effects into the ray-tracing engine.

1. Introduction

Millimeter wave (mm-wave) frequencies are being considered for fifth generation (5G) and beyond mobile wireless communications due to the availability of free bandwidth and other desirable characteristics (Rappaport et al., 2013; Salous et al., 2016). Mm-wave spectrum will definitely support higher data rate transmission and allow the implementation of Massive MIMO and beamforming schemes, to optimize system performance and achieve a high throughput density. Among all frequencies under consideration within the World Radio Conference 2019 Agenda Item 1.13 (WRC-19 A.I. 1.13), in accordance with Resolution 238 WRC-15 (*World Radiocommunication Conference*, Geneva (CH), November 2015), the Ka band (26.5–40 GHz) has attracted particular attention as a candidate for urban microcells, also boosted by the European Commission's 5G Action Plan (*EU law and publications*, Bruxelles, 14/09/2016, 2016), which has identified the spectrum at 24.25–27.5 GHz as the “pioneer” mm-wave band for Europe (*Radio Spectrum Policy Group*, Brussels, 09 November 2016) and by the FCC's 5G fast plan (*Federal Communications Commission*, Washington D.C., 28/09/2018, 2018), which includes among other key topics, actions to make additional spectrum available for 5G services. While mm-wave frequencies offer much higher bandwidths, they suffer from isotropic path-loss and higher blocking due to obstacles such as buildings, trees, and terrain when compared to the lower frequency bands currently used in mobile networks (Salous et al., 2016). Connectivity in non-line-of-sight (NLOS) conditions has traditionally relied on multipath propagation, which is nevertheless not as effective at higher frequencies due to lower diffraction effects, and whether mm-wave communications will work in NLOS conditions in practical deployments still needs to be fully understood. Considerable effort has been spent in recent years in the characterization of mm-wave propagation, both in indoor (Ai et al., 2017; Fuschini et al., 2017; Inomata, Imai, et al., 2017; Inomata, Sasaki, et al., 2017; Cheng et al., 2017; Huang et al., 2016; Nielsen & Pedersen, 2016; Karstensen et al., 2016) and in outdoor scenarios (Rappaport, Xing, et al., 2017; Sun et al., 2018; Weiler et al., 2016; Rappaport, MacCartney, et al., 2017; Rappaport et al., 2015; Leonor et al., 2014; Solomitckii et al., 2016; Zhong et al., 2017; Park et al., 2016; Hur et al., 2015). Among the latter, some papers are comprehensive surveys on mm-wave communications (Rappaport, Xing, et al., 2017) or on mm-wave propagation models for 5G systems (Rappaport et al., 2015); others deal with narrowband path-loss or shadowing models (Rappaport, MacCartney, et al., 2017; Weiler et al., 2016) or with wideband mm-wave models (Rappaport et al., 2015; Hur et al., 2015; Park et al., 2016). Very few papers address peculiar characteristic of outdoor mm-wave propagation such as the effect

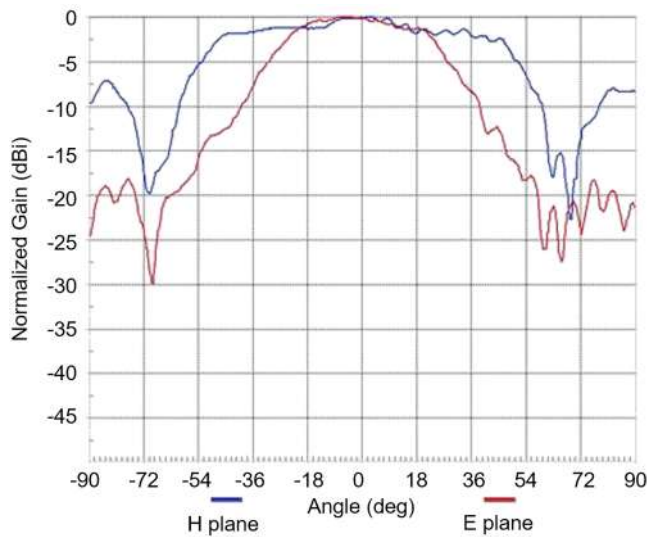


Figure 1. 2-D radiation patterns of the Tx directional antenna used in the measurements.

consider attenuation by vegetation and diffuse scattering from surface and material irregularities at mm-wave frequencies, then tested versus measurements. Challenging outdoor urban scenarios are considered, with the presence of vegetation and cluttering (lamp posts and parked cars). With respect to preliminary work shown in Mani et al. (2018), the analysis here is improved and extended to an additional urban scenario with mid-rise buildings, little vegetation, and a street with cars, an additional frequency, and different transmitter antenna heights (see section 2.1). Results show that diffuse scattering from building walls and objects close to them (signs, poles, etc.) is much more relevant than expected even when only narrowband radio frequency (RF) coverage is considered, especially in NLOS locations. This contrasts with previous work on sub-6 GHz propagation, where nonspecular scattering was found to have an important impact on wideband propagation parameters, but a minor one on narrowband outdoor coverage except for specific cases (Degli-Esposti et al., 2004). Vegetation attenuation is also very relevant, as highlighted in previous work Leonor et al. (2014), and can be modeled using the 3-D vegetation polygons available in most ESRI-SHAPE building databases (*ESRI Company*, July 1998) using a simple specific attenuation formula. Moreover, a preliminary analysis is carried out on the effect of back-scattering from cars, modeled as simple metal sheets with a given curvature, to understand whether their contribution can explain the

presence of RF coverage in some deep-NLOS locations, where RT prediction suffers from an underestimation of over 20 dB if the sole building database—without cluttering objects—is considered. This paper is organized in the following way: Section 2 describes the considered urban scenarios and the measurement campaigns, Section 3 describes the RT model and its features, Section 4 presents and analyzes measurement and RT simulation results, while Conclusions are drawn in Section 5.

2. Scenarios and Measurement Campaigns

Measurements were carried out in Shanghai (China) in two different scenarios: Tengfei, an office district, and the Shanghai Jiao Tong University campus (SJTU). In both cases, the base stations (BS) were elevated with respect to ground and employed a directional horn transmitting (Tx) antenna with a gain of about 8.3 dBi, while the receiving (Rx) unit employed an omnidirectional antenna located at 1.5 m from the ground level. The 2-D radiation patterns of the antennas in the E and H planes are shown in Figure 1 and 2 for the directive and omnidirectional antennas, respectively. The horn antenna has a half-power beam width in the horizontal plane of about 110°, which emulates quite well a typical sector antenna of a cellular site. The Tx unit of the channel sounder consisted

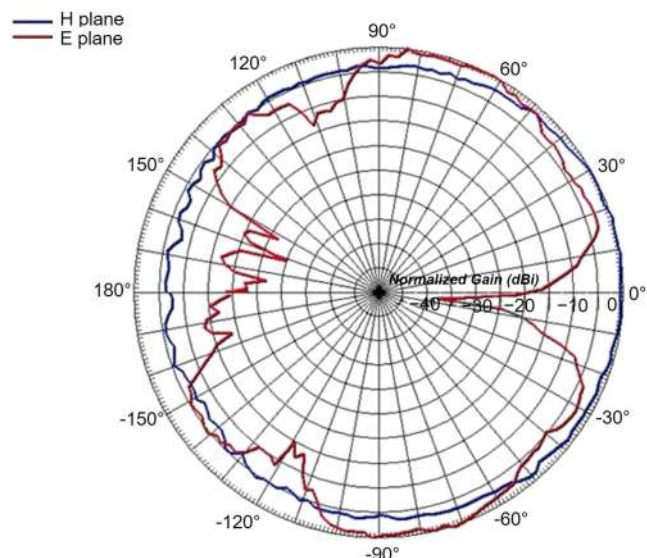


Figure 2. 2-D radiation patterns of the Rx omnidirectional antenna used in the measurements.

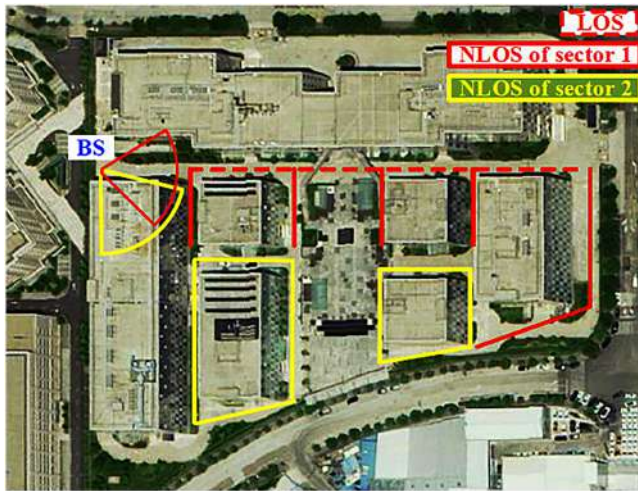


Figure 3. Aerial pictures of the Tengfei measurement scenario, including BS and Rx routes.

of a Keysight 4438C signal generator with 350 MHz bandwidth connected to an up-converter module and a high-gain power amplifier operating in the 26-40 GHz band, while at the Rx unit a Keysight N9030B signal analyzer was used. More details on the measurement equipment can be found in Zhong et al. (2017).

2.1. Tengfei Scenario

This scenario, depicted in Figure 3, is an office park that can be compared to a modern urban scenario with little vegetation and including complex structures as pedestrian bridges and ark-shaped buildings. The BS antenna with the Tx equipment was placed on a lift platform at four different heights: 5 m, 10 m, 14 m, and 17 m (see Figure 4). Since the BS height was always below the average building height, the measurement scenario can be regarded as typical urban microcellular scenario. The receiving User Equipment (UE) was installed on a trolley that traveled along multiple routes both in line-of-sight (LOS) and in NLOS conditions. Along each route, static measurements were recorded in different locations, with a distance of about 2 m between adjacent positions. All the

measurement locations were referenced using GPS. Moreover, the BS antenna was pointed in two different directions corresponding to two different groups of measurement routes (red and yellow lines in Figure 3), in order to have the radial line connecting BS and UE always falling within the main beam of the Tx antenna. Two measurement frequencies were used for this scenario: 28 and 38.6 GHz.

2.2. SJTU Scenario

The second scenario, depicted in Figure 5, is a University campus with more traditional buildings but surrounded by abundant vegetation. The BS was placed on top of a low building at 10 m from the ground. The UE was always located in NLOS condition with the radial path blocked either by buildings or vegetation. Also in this case, the BS antenna was rotated to keep the main radiation lobe pointed toward the UE moving along different measurement routes (white lines in Figure 5). The operation frequency is in this case 26 GHz.

3. The Model and its Extended Features

The employed model is an advanced 3-D RT tool (Fuschini et al., 2015), which is able to model propagation in outdoor environments through multiple interactions, including specular reflection, transmission, diffraction modeled through the uniform theory of diffraction (Kouyoumjian & Pathak, 1974; Balanis, 1989), and diffuse scattering modeled through the Effective Roughness (ER) method (Degli-Esposti et al., 2007). Any combination of the different interaction types is possible. Anyway, the maximum number of interactions in the same ray is limited to four reflections and two diffractions, while diffuse scattering is limited to a

single bounce, due to computation time constraints. Transmission is neglected in RT simulations except for vegetation polygons, according to the usual practice for outdoor environment. The RT model is also able to consider multiple diffractions on building rooftops, which can be important in NLOS situations. Due to theoretical limitations in the rigorous computation of the diffracted field for arbitrarily oriented wedges using the approach, in the RT model the over-roof-top contribution is computed through a heuristic, simplified approach (Vitucci et al., 2018; ITU-R, 2013; Epstein and Peterson, 1953). Over-roof-top (as diffraction in general) is not expected to be very important at the Ka band frequencies compared to other interaction mechanisms, anyway.

With respect to standard RT, the additional features shortly outlined in the following subsection are implemented in the RT model used in this work. In the following subsection, short descriptions of the extended features that are relevant to the present work are provided.

3.1. Extended Features

When extending RT capabilities to propagation mechanisms not taken into account by traditional geometrical optics, one of the major problems



Figure 4. BS and UE configuration during the measurement in Tengfei scenario.



Figure 5. Aerial pictures of the SJTU measurement scenario, including BS and Rx routes.

is to identify simple and yet sound models that can be easily embedded into the tracing engine and that require the same, simplified environment description based on commonly used format such as the ESRI Shapefile Format (ESRI Company, July 1998). According to this format, buildings and vegetation blocks are stored as polygons with an associated height to derive right prisms—that is, polyhedrons with polygonal base and ceiling, parallel to each other—having the same height as the buildings or trees they represent. For the case of nonspecular scattering, the ER model has been conceived specifically for ray-based propagation models (Degli-Esposti et al., 2007), while for vegetation attenuation we considered two simple models that could be easily implemented in the RT engine, as described below.

3.1.1. Diffuse Scattering

According to the ER method (Degli-Esposti et al., 2007), diffuse scattering due to deviations in building walls from being smooth, uniform layers—and therefore including the effect of structures not present in the building database such as signs, columns, decorations, window frames, and so forth—is generated by dividing the walls into surface elements (tiles). Diffuse rays are supposed to originate from the centre of each of these tiles. The model assigns an amplitude scattering coefficient S and scattering pattern model to each surface. S sets the amount of scattered power, and this is linked to a reduction factor of the specular rays $R = \sqrt{1 - S^2}$, which sets the amount of power subtracted by diffuse scattering to specular reflection. The diffused field from a surface element dS is computed as

$$|E_s(r_s, \theta_s)|^2 = \frac{E_{s0}^2}{F_{\alpha_r}} \left(\frac{1 + \cos\psi_r}{2} \right)^{\alpha_r} \quad (1)$$

$$\text{with } E_{s0}^2 = \left(\frac{K_0 \Gamma S}{r_i r_s} \right)^2 \cdot \cos\theta_i,$$

where K_0 is a function of the transmitting antenna gain, S is the scattering coefficient, r_i and r_s are the lengths of the incident and of the scattered rays, respectively, θ_i and Γ are the angle of incidence and the corresponding reflection coefficient, F_{α_r} is a coefficient that can be found in Degli-Esposti et al. (2007), ψ_r is the angle between the reflection and scattering directions, and α_r is a coefficient that sets the width of the scattering lobe. In the following, $\alpha_r = 2$ is assumed, which gave the best results in previous studies in outdoor scenarios at lower frequencies (Mani & Oestges, 2011).

3.1.2. Attenuation by Vegetation

As vegetation may be present in many outdoor environments, its effect must be taken into account. Some models for vegetation scattering and absorption have been presented in the literature based on propagation

Table 1 Simulation Parameters	
Sim. parameter	value
Transmitted power [dBm]	34
Relative permittivity	5.3
Conductivity [S/m]	0.4
Scattering parameter S	0.6
Max. number of reflections	4
Max. number of diffractions	2
Max. number of reflections and diffractions combined	2
Max. number of reflections combined with scattering	1
Average simulation time (minutes) - Tengfei scenario	70
Average simulation time (minutes) - SJTU scenario	720

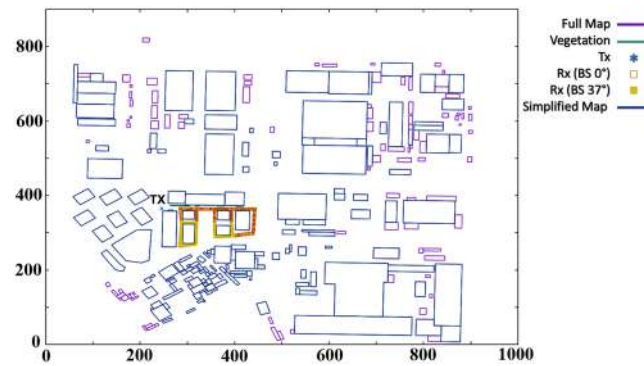


Figure 6. 2-D map of the simulated Tengfei scenario, including buildings, vegetation polygons, and Tx/Rx locations.

in random media (Leonor et al., 2014; ITU-R, 2016). Such models consider both scattering and attenuation from trees, but while the latter is simple to model and certainly important at mm-wave frequencies, the former is difficult to implement into a ray-based model as commercially available environment databases usually contain generic polygons of vegetated areas (parks, flowerbeds, roadside trees, etc.) but very rarely information on the exact location, size, and characteristics of each tree. The ITU 833-9 model (ITU-R, 2016) is very useful for RF coverage prediction in large vegetated areas of well-defined characteristics, but requires a number of parameters such as the ratio of the forward scattered power to the total scattered power, that are not available for vegetation polygons in urban databases. Moreover, backscattering from trees, being generated in random sparse media, is most probably weaker than scattering from objects such as cars and lampposts, where incoming waves are totally backscattered by curved metal surfaces. Therefore, we decided to take into account the vegetation effect simply as an excess loss applied to each ray intersecting one or more vegetation volumes, depending on the length of each ray section inside vegetation polygons, assumed as semitransparent solids made of a lossy isotropic media. Backscattering from vegetation polygons is neglected in the present work. Two simple models for vegetation loss have been considered. The first one is the well-known Weissberger model (Weissberger, 1982), which covers a frequency range between 230 MHz and 95 GHz and a penetration depth up to 400 m. Its formulation for a loss in dB is the following:

$$L_v = \begin{cases} 1.33 f^{0.284} d^{0.588} & 14 < d \leq 400 \\ 0.45 f^{0.284} d & 0 < d \leq 14, \end{cases} \quad (2)$$

where f is the frequency in GHz and d is the total ray path length inside vegetation expressed in meters. The second one is a simple model where the specific attenuation γ (dB/m) is multiplied by the distance traveled by the ray inside vegetation: $L_v = \gamma d$. Typical values of γ can be found in literature. As an example, in de Jong and Herben (2004), $\gamma = 1$ dB/m is considered for 2 GHz propagation, but γ strongly depends on the simu-

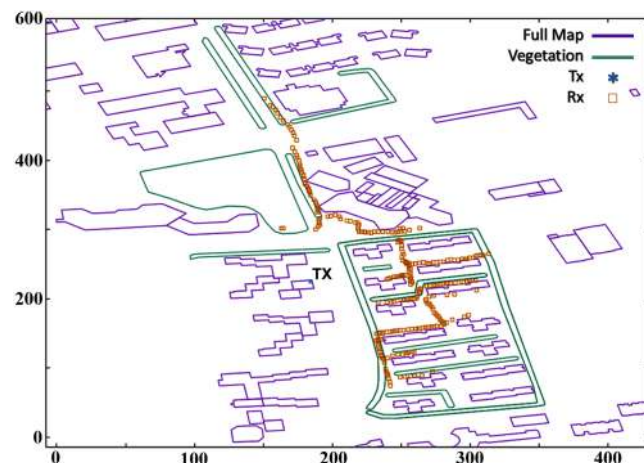


Figure 7. 2-D map of the simulated SJTU scenario, including buildings, vegetation polygons, and Tx/Rx locations.

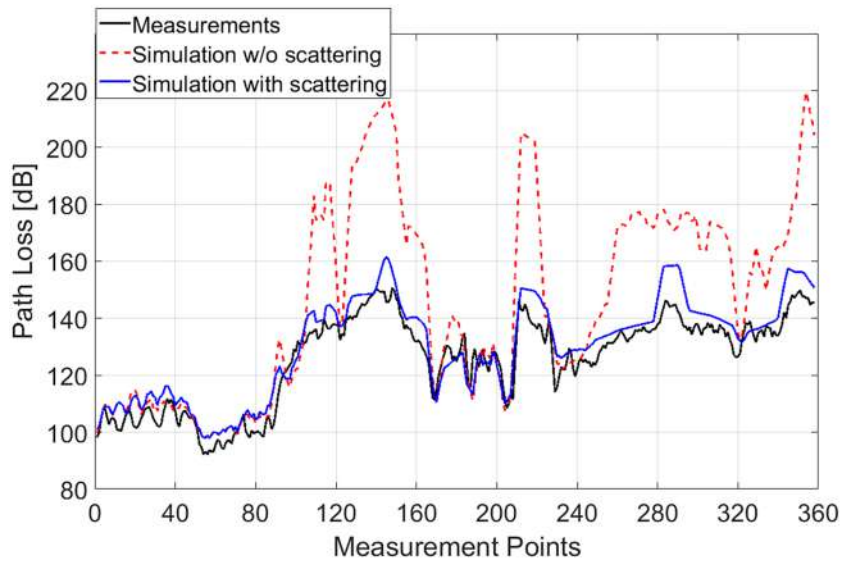


Figure 8. Comparison of measurements with simulations with and without scattering in Tengfei scenario at 28 GHz and for $h_{BS} = 5\text{m}$.

lation frequency. In Goldhirsh and Vogel (1998), the following frequency scaling formula for attenuation in dB is proposed:

$$L_v(f_2) = L_v(f_1) \sqrt{\frac{f_2}{f_1}}, \quad (3)$$

where f_2 is the target frequency and f_1 is the original frequency where the excess loss $L_v(f_1)$ is assumed known.

4. Measurement and Simulation Results

4.1. Simulation Parameters and Validation Metrics

Table 1 presents the simulation parameters used in the two scenarios, where the number and type of bounces are chosen to provide a good trade-off between prediction accuracy and simulation time. A calibration of the building material parameters (relative permittivity ϵ_r and conductivity σ) has been carried out, in particular initial values of the parameters in the Ka band were derived from a literature survey (Salous et al., 2016;

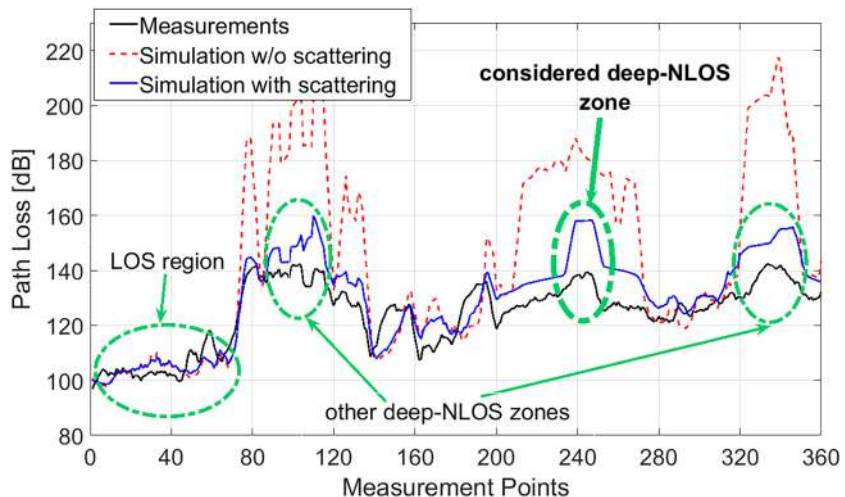


Figure 9. Comparison of measurements with simulations with and without scattering in Tengfei scenario at 28GHz and for $h_{BS} = 10\text{m}$.

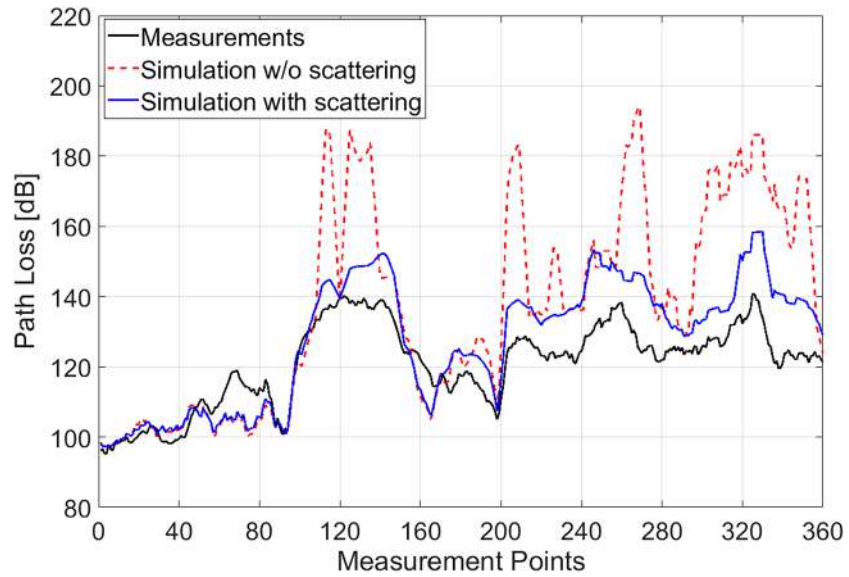


Figure 10. Comparison of measurements with simulations with and without scattering in Tengfei scenario at 28GHz and for $h_{BS} = 14\text{m}$.

Fuschini et al., 2016), and then, a finer tuning was performed versus measurements, yielding to the following optimum values: $\epsilon_r = 5.3$, $\sigma = 0.4 \text{ S/m}$. Figure 6 presents 2-D map of the Tengfei simulated scenario while Figure 7 presents 2-D map of the SJTU simulated scenario. The available input database, as it is often the case for maps of large scenarios, did not include some details, for example, pedestrian bridges and vegetation polygons in Tengfei and some minor buildings in SJTU. When possible, this was overcome by hand-drawing the missing building or vegetation blocks, after visual inspection of the scenario. The reference metric is normalized path loss (PL), defined in dB as

$$PL = P_t - P_r + G_t + G_r, \tag{4}$$

where P_t is the transmitted power, P_r is the received power, and G_t and G_r are the transmitting and receiving antenna gains, respectively. Local averages have been considered for both the measured and the

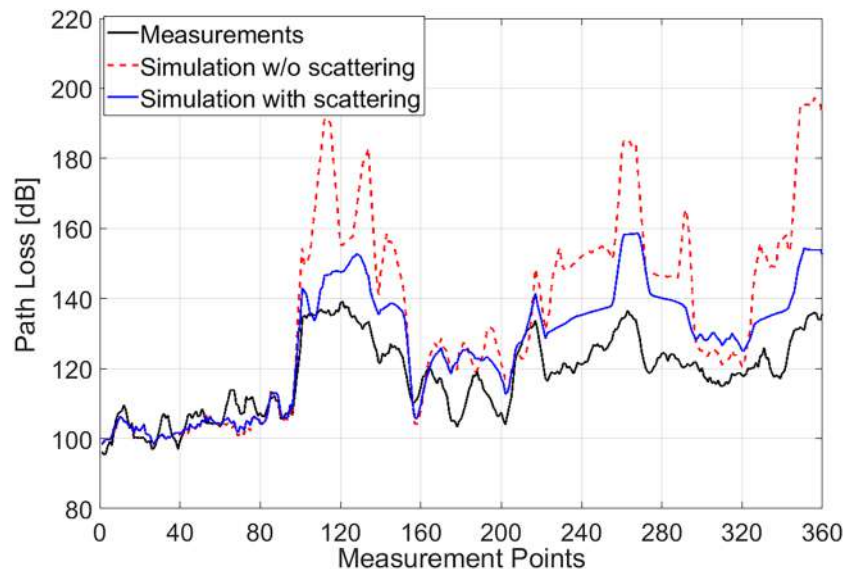


Figure 11. Comparison of measurements with simulations with and without scattering in Tengfei scenario at 28GHz and for $h_{BS} = 17 \text{ m}$.

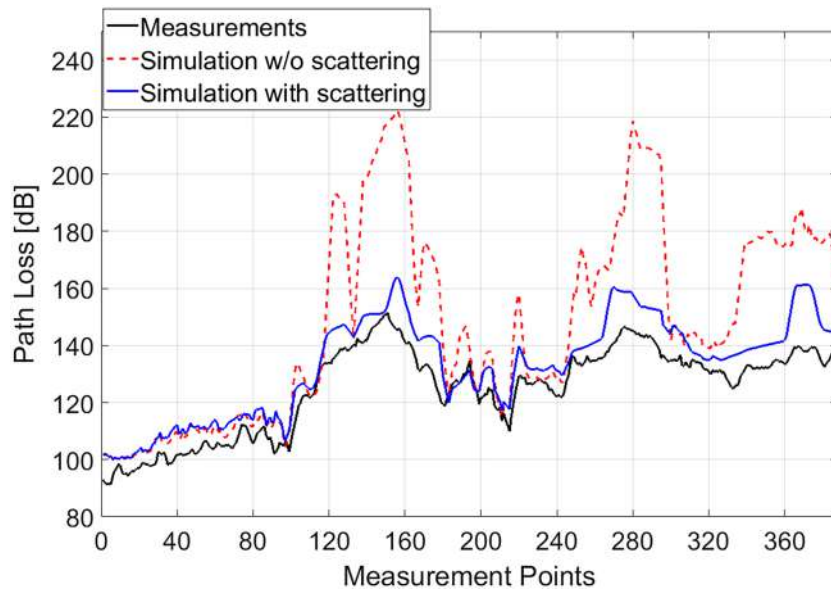


Figure 12. Comparison of measurements with simulations with and without scattering in Tengfei scenario at 38 GHz and for $h_{BS} = 5$ m.

RT-simulated PL values by applying a 5-m wide averaging sliding window on samples along the considered routes.

4.2. Results in Tengfei Scenario

Figures 8–11 present the simulated PL compared with measurements for different Tx heights (from $h_{BS} = 5$ m to $h_{BS} = 17$ m) at 28 GHz, and, in particular, the contribution of diffuse scattering is highlighted by showing simulation results when this feature is enabled or not. The results clearly show the importance of this type of interaction to get a realistic prediction in deep NLOS positions where most of the received power comes from nonspecular contributions, that is, diffuse scattering. Deep NLOS locations are Rx positions where the LOS path is obstructed by at least two buildings, that is, Rx route sections facing the curved street at the bottom of Figure 3. This result was somehow unexpected, since previous studies at

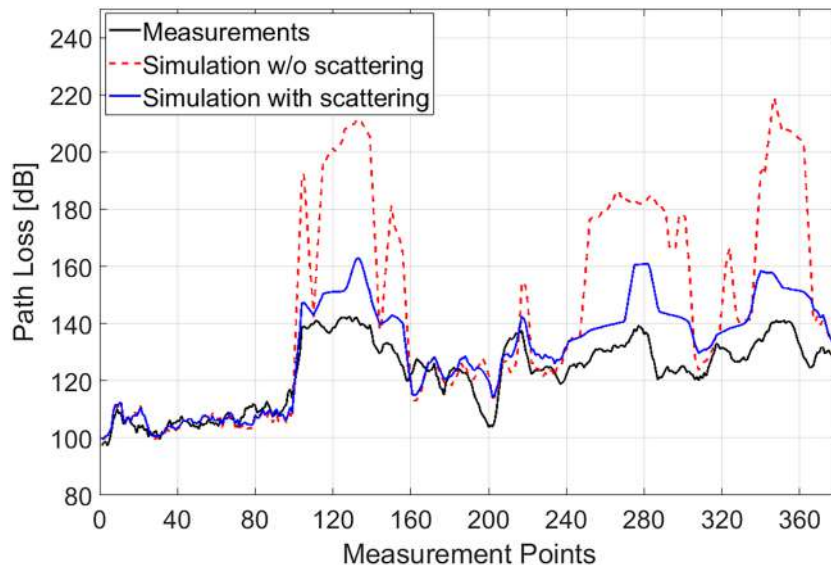


Figure 13. Comparison of measurements with simulations with and without scattering in Tengfei scenario at 38 GHz and for $h_{BS} = 10$ m.

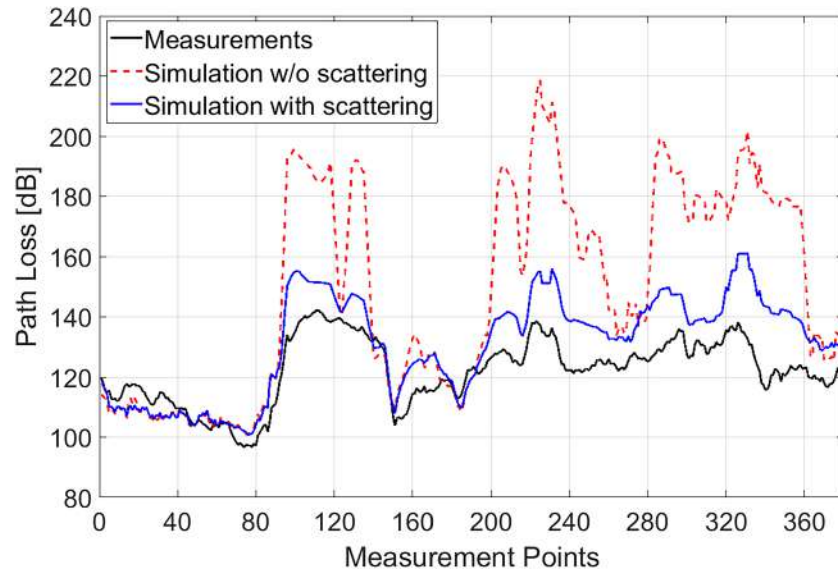


Figure 14. Comparison of measurements with simulations with and without scattering in Tengfei scenario at 38 GHz and for $h_{BS} = 14$ m.

lower frequencies have highlighted that diffuse scattering is important to model the temporal/angular dispersion characteristics of the channel such as delay spread and angle spread (Fuschini et al., 2008; Degli-Esposti et al., 2009), rather than for PL prediction. Recent studies on outdoor propagation at mm-wave frequencies have actually shown the importance of nonspecular scattering, but to a lesser extent than what found here (Solomitckii et al., 2016). It is interesting to note that the shape of the measurement curve is well reproduced by simulations with scattering even where PL is overestimated by simulations. A rigorous comparison of the plots for different Tx heights is not possible, because during the measurements the NLOS streets were traveled by the mobile terminal each time in a slightly different way. However, in all cases, we observe that the overestimation of the PL in NLOS locations is slightly increasing with Tx height. In a similar way, Figures 12–15 present the results at 38 GHz for different Tx heights (from $h_{BS} = 5$ m to $h_{BS} = 17$ m). The measured and simulated PL values appear to be similar to, or slightly higher than, the 28 GHz case, as they should since the expected PL difference for the LOS component only at the two frequencies can be computed as

$$\Delta_{PL}[dB] = 20\log_{10}\left(\frac{38.6}{28}\right) = 2.8 \text{ dB}. \quad (5)$$

The quality of the prediction is on average similar to the other frequency, and the contribution of diffuse scattering is equally—if not more—decisive. This is in agreement with previous studies that found propagation at the two very same frequencies to show very similar characteristics (Park et al., 2016). Tables 2

Table 2
Summary of Prediction Errors [dB] in Tengfei Scenario When Scattering is Included in the Simulations

	Mean Error	Standard Deviation	RMSE
f = 28 GHz $h_{BS} = 5$ m	-4.4	4.4	6.2
f = 28 GHz $h_{BS} = 10$ m	-5.3	7.2	8.9
f = 28 GHz $h_{BS} = 14$ m	-6.8	7.9	10.4
f = 28 GHz $h_{BS} = 17$ m	-9.3	8.2	12.4
f = 38 GHz $h_{BS} = 5$ m	-7.9	4.6	9.1
f = 38 GHz $h_{BS} = 10$ m	-7.6	7.9	11.0
f = 38 GHz $h_{BS} = 14$ m	-8.9	8.1	12.1
f = 38 GHz $h_{BS} = 17$ m	-10.5	8.0	13.2

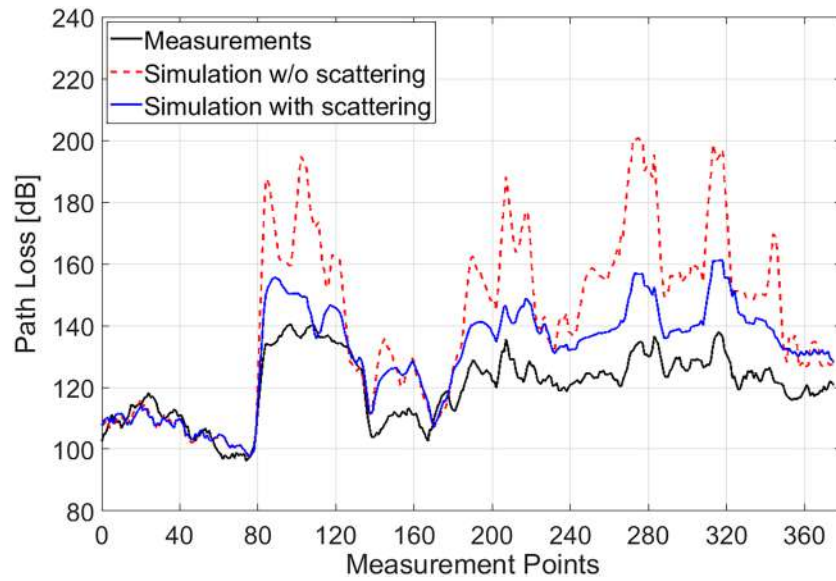


Figure 15. Comparison of measurements with simulations with and without scattering in Tengfei scenario at 38 GHz and for $h_{BS} = 17$ m.

and 3 summarize the prediction errors in Tangfei Scenario for both frequencies, when scattering is included (Table 2) and not included (Table 3) in the ray-tracing tool. Since diffuse scattering appears to be a very important feature in NLOS locations at mm-wave frequencies, we also tested the simulation versus measurements for different values of the scattering parameter S . While diffuse scattering components become more powerful with S , specular reflection attenuates according to reduction factor $R = \sqrt{1 - S^2}$. Therefore, the dependence of PL on S is not trivial. We also tested $S = 1$ as a reference, extreme case where building surfaces would act as pure sources of diffuse scattering and no specular reflection would occur. Figure 16 shows a comparison between measurements and simulations for different values of S in the range $[0.4 - 1]$, considering the case of 28 GHz and $h_{BS} = 14$ m. Table 4 shows the related RMSE values. According to the errors, optimal values seem to range between 0.6 and 0.8. Similar results have been obtained for different antenna heights and for the higher frequency. $S = [0.6 \div 0.8]$ are quite high values compared to what found in previous studies at lower frequencies (Degli-Esposti et al., 2007; Mani & Oestges, 2011). An explanation could be that outdoor construction materials such as bricks, cement, asphalt, and so forth have a roughness standard deviation comparable to the wavelength at mm-wave frequencies and therefore generate considerable nonspecular scattering. Another possible explanation can be that high-scattering coefficient values might compensate other issues, that is, inaccuracies in the geometrical input database or some contributions RT could not reproduce that caused a PL overestimation in most NLOS locations. Such faults are more evident at mm-wave frequencies because of the relative lack of diffraction and over-roof-top compensating contributions. However, it is interesting to note that PL overestimation tends to increase with the Tx height. In fact, since the Tx antenna is quite directive in the vertical plane, most of the power tends to remain on a plane at the same height as the Tx even after multiple reflections on vertical build-

Table 3
Summary of Prediction Errors [dB] in Tengfei Scenario When Scattering is Excluded From the Simulations

	Mean Error	Standard Deviation	RMSE
f = 28 GHz $h_{BS} = 5$ m	-20.8	20.9	29.5
f = 28 GHz $h_{BS} = 10$ m	-19.5	24.1	30.1
f = 28 GHz $h_{BS} = 14$ m	-15.8	19.7	25.2
f = 28 GHz $h_{BS} = 17$ m	-18.4	18.4	26.0
f = 38 GHz $h_{BS} = 5$ m	-24.2	21.4	32.2
f = 38 GHz $h_{BS} = 10$ m	-21.0	25.6	33.1
f = 38 GHz $h_{BS} = 14$ m	-26.5	25.8	37.0
f = 38 GHz $h_{BS} = 17$ m	-21.5	18.7	28.5

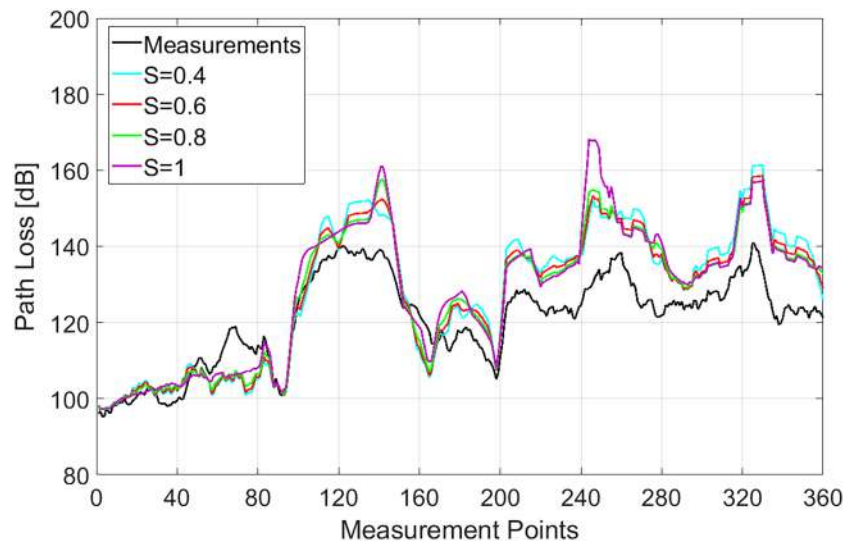


Figure 16. Tengfei scenario: Comparison of measurements and simulations with different values of the Scattering coefficient (28 GHz, $h_{BS} = 14$ m).

ing walls, and probably such multiple reflections can reach NLOS or even deep-NLOS locations, partially compensating the lack of other contributions. Conversely, when the Tx antenna is much higher than the Rx, multiple reflections do not help much. Even with the addition of diffuse scattering, RT simulations still overestimate PL in most NLOS locations. This might be due to the presence of cluttering objects (e.g., cars, lampposts, etc.) which are actually present in the environment, but not considered in RT simulations. This effect is clearly visible if we refer for instance to the deep-NLOS zone highlighted in Figure 9 (green dotted circle, “considered deep-NLOS zone”) and Figure 17 (red circle): since the Tx is facing a street with parked cars, the Rx locations can be reached through a single bounce from such cars (see Figure 17, 18). If the cluttering objects contribution is not considered, simulations overestimate the path loss by 20 dB on average. Increasing the number of bounces does not help much: we tried to increase the number of reflections from four to eight (with an increase of the computation time from 70 min to about 1 day), but we got an improvement of the predicted power of less than 1 dB. On the other hand, if we take somehow into account the cars, we can easily achieve a PL similar to the measurements. In order to prove that, let us consider the scenario of Figure 17 and the formulation for reflection from a perfect electric conductor curved surface with principal curvature radii R_1 and R_2 , as detailed in Appendix A. For the considered car and NLOS locations, distances are $\rho_i=150$ m, $s=80$ m (see Figure 17). If we consider as a proxy for the car surface a spherical surface of radius 2.8 m, that is, $R_1=R_2=2.8$ m, which can represent the low-curvature hood or side surface of a car, from equation (A3) of Appendix A we get $PL = 140$ dB, that is, exactly the average measured path loss shown in Figure 9 for the considered deep-NLOS location. This means that the car model reflection is 100 times stronger than all the other contributions predicted by the RT tool. The chosen curvature radius value is probably excessive and unrealistic for a car, but in this simplified calculation we are considering the effect of a single car only, while in reality there is an effect that is the combination of multiple reflections caused by several cars. On the other hand, if we modeled backscattering from cars as reflection from a flat surface, we would get $PL = 120$ dB, that is, we would overcompensate the attenuation by about 20 dB. In order to

Table 4
Comparison of RMSE for Different Values of Scattering Coefficient in the Tengfei Scenario (28 GHz, $h_{BS} = 14$ m)

	S=0.4	S=0.6	S=0.8	S=1	S=0 (no scat)
RMSE	11.17	10.39	10.41	11.62	25.2



Figure 17. Tengfei scenario: Considered deep-NLOS location.

model the effect of the car reflection in a more realistic manner, we should consider surfaces with a double curvature, instead of spherical surfaces. Large and low-curvature surfaces such as the hood and the side of a car can generate a relatively strong reflection but a very directive reflection cone; therefore, such a reflection can only take place for small set of car orientations and therefore is unlikely to actually occur. On the other hand, surfaces with one high-curvature direction such as the upright rod of a car's windshield are probably much more likely to generate reflection for a wide angular range. To investigate this case, let us consider an upright rod oriented at 45 degrees to the ground, with $R_1 = 15$ m and $R_2 = 0.5$ m, $\theta_1 = \pi/2$, $\theta_2 = \pi/2 - \theta_1$. Using again the formulation of Appendix A, we get $PL = 140$ dB, again the same value as in Figure 9. Just to have an idea of the potential improvement, even with this simple off-line model and by repeating the same calculation for all deep-NLOS locations corresponding to case of Figure 9, the average prediction error can be reduced from -5.3 dB to about -2 dB, while RMSE is reduced from 9 dB to about 7.5 dB. Therefore, we can infer that by modeling in a simplified way cluttering objects such as cars where they are expected to be present—for example, in parking lots and along busy streets—and embedding such models into the RT prediction tool, much better error statistics could be achieved with respect to what reported in tables and figures above. This idea will have to be fully developed in future work.

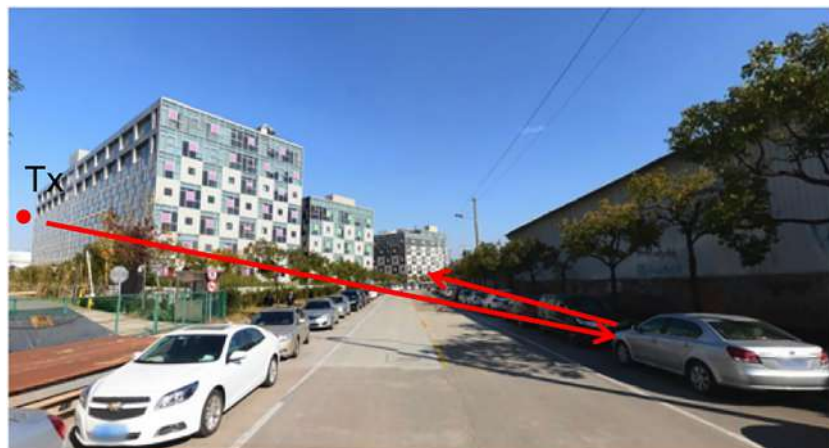


Figure 18. Tengfei scenario: Contribution of reflecting cars.

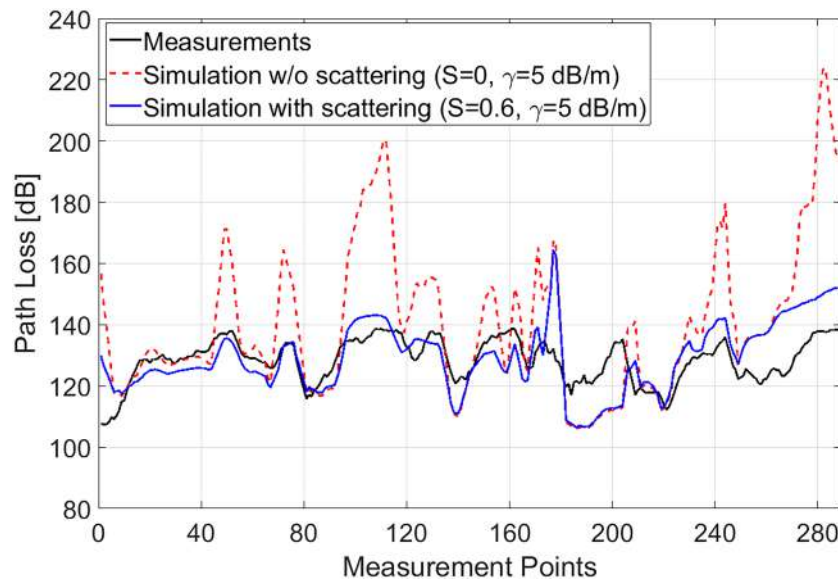


Figure 19. SJTU scenario: Comparison between measurements and simulations when diffuse scattering is included or not in the simulations.

4.3. Results in SJTU Scenario

The first result, presented in Figure 19, shows once again the importance of diffuse scattering, similar to what we have found in the Tengfei scenario. As a matter of fact, in deep NLOS locations, diffuse scattering is decisive to achieve good prediction capability. By properly modeling attenuation by vegetation, a RMSE error equal to 7.3 dB is achieved. Also in this case, satisfactory results are obtained assuming $S = 0.6$. Figure 20 presents simulation results with and without vegetation attenuation and a comparison between the two vegetation attenuation models is introduced in section 3.1. As it could be expected, not including vegetation yields a significant underestimation of the PL. Also, the Weissberger model appears to yield an underestimation. Therefore, we can conclude that a specific loss model is more suitable for the considered scenarios at the Ka-band frequencies. As a starting point, we have considered $\gamma = 5$ dB/m, by applying equation (3) and considering a specific loss of 1 dB/m at 2 GHz (de Jong & Herben, 2004). As we can see in Figure 21, we

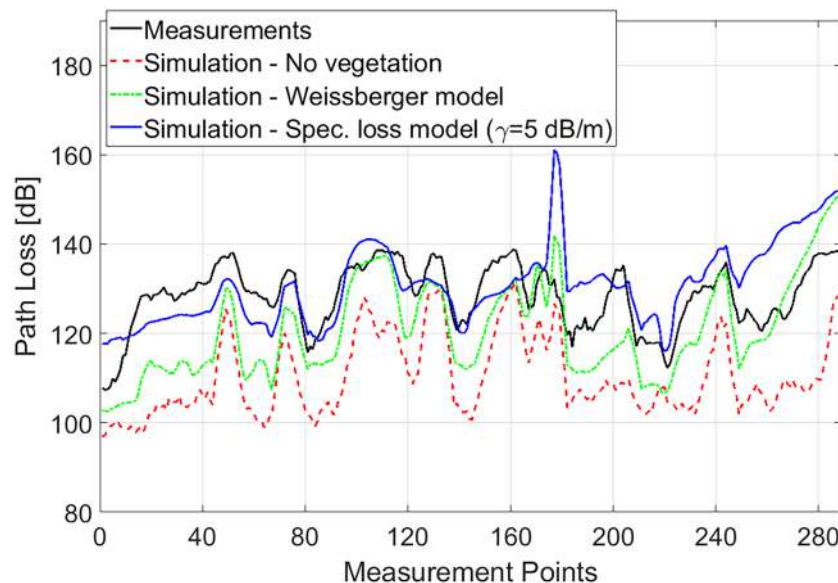


Figure 20. Comparison of measurements and simulations with and without vegetation in SJTU scenario.

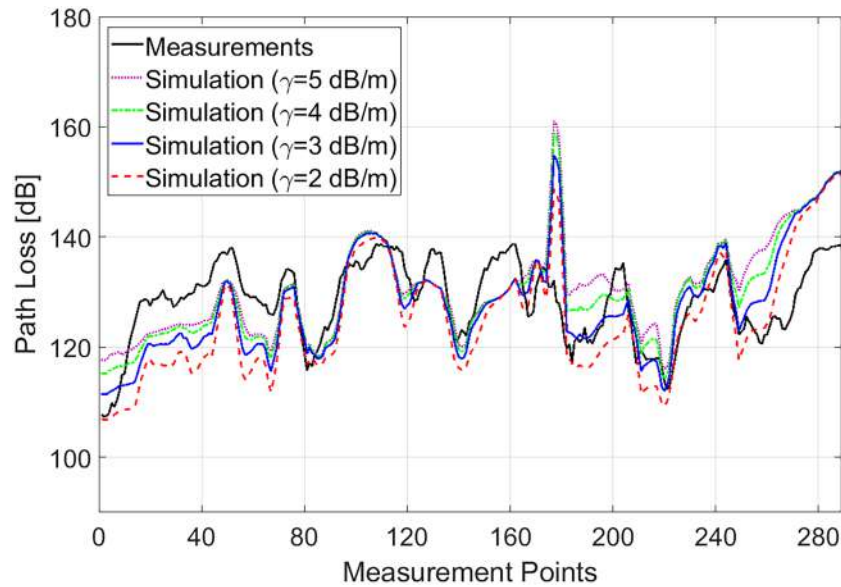


Figure 21. Comparison between measurements and simulations with different excess vegetation loss models in SJTU scenario.

tend to overestimate PL with this level of specific loss, so we also tested lower values. Table 5 summarizes the prediction errors for both models and different values of specific attenuation. The RMSE of the four tested values differs only by fractions of dB. Nevertheless, while 5 dB/m seems to overestimate the vegetation loss and 2 dB/m to underestimate it, we can safely assume that values between 3 and 4 dB/m can be considered suitable for this kind of scenario at these frequencies. Note that this value of specific attenuation is much lower than what found in other investigations, such as in Leonor et al. (2014) where the parameter Att_k is found to lay in the range 10 to 20 dB/m depending on the kind of tree. In our case however, we consider attenuation through a "vegetation polygon" not through a single tree. Vegetation polygons in the environment database refer to vegetated areas in cities where trees probably occupy less than 50% of the area and 20% of the volume, and this can explain the discrepancy of the specific attenuation figures.

5. Conclusion

This work is on the improvement and tuning of a RT model versus measurements in outdoor scenarios in the Ka band. By considering a modern office-building scenario with little vegetation (Tengfei) and a university campus scenario with copious vegetation (SJTU), we could analyze the impact of different propagation characteristics. We have shown that both diffuse scattering from buildings and objects, and attenuation from vegetation, can have a relevant impact for RF-coverage analysis at mm-wave frequencies, and we believe these findings have great importance for the design and the deployment of present and future mm-wave transmission systems. In particular, properly modeling diffuse scattering from building walls appears to be decisive—much more than we expected—to get realistic prediction results in NLOS conditions, even just considering narrowband RF coverage. Moreover, even if prediction accuracy is sufficiently good, with

	Mean Error	Standard Deviation	RMSE
No Vegetation	18.0	6.2	19.0
Weissberger	7.5	7.3	10.5
Specific Att. 5 dB/m	-2.4	8.0	8.3
Specific Att. 4 dB/m	-1.3	7.6	7.7
Specific Att. 3 dB/m	0.5	7.3	7.3
Specific Att. 2 dB/m	3.3	7.4	8.1

an average RMSE of the order of 8 – 9 dB, further improvements seem possible if the presence of cluttering, for example, parked cars, is considered in the simulations, according to a preliminary evaluation we have shown in the paper. The analysis of attenuation by vegetation in the SJTU scenario suggests that a properly tuned specific attenuation model can provide good results. Specific attenuation values between 3 and 4 dB/m applied to all rays going through vegetation polygons give the best results at the considered frequencies. A systematic modeling of scattering from cluttering objects, which will be developed through a wideband analysis of experimental results, will be object of future work.

Appendix A: Reflection from a PEC Curved Surface

In this Appendix, we compute the contribution of a single-bounce reflection from a perfect electric conductor (PEC)-curved surface that approximates a car's metal body surface. It is known that the generic-curved surface at every point has two principal directions corresponding to two different principal curvature radii R_1, R_2 . Assuming that a far-field spherical wave with curvature radius ρ_i reflects on the curved surface, with θ_i the incidence angle and θ_1, θ_2 the angles between the incidence direction and the two principal directions, the reflected wave is an astigmatic wave with curvature radii ρ_r^1, ρ_r^2 (see Kouyoumjian & Pathak, 1974, Appendix I):

$$\frac{1}{\rho_r^{1/2}} = \frac{1}{\rho_i} + \frac{1}{\cos \theta_i} \left[\frac{\sin^2 \theta_1}{R_2} + \frac{\sin^2 \theta_2}{R_1} \right] + \pm \sqrt{\frac{1}{\cos^2 \theta_i} \left[\frac{\sin^2 \theta_1}{R_2} + \frac{\sin^2 \theta_2}{R_1} \right]^2 - \frac{4}{R_1 R_2}}, \quad (\text{A1})$$

in which the plus sign is associated with ρ_r^1 and the minus sign with ρ_r^2 . The spreading factor of the reflected wave at a distance S from the surface can be therefore expressed as (Balanis, 1989)

$$SF = \frac{\rho_r^1 \rho_r^2}{(\rho_r^1 + s)(\rho_r^2 + s)}, \quad (\text{A2})$$

and the overall dB path-loss from the source to the receiving point, at a distance S from the PEC surface, can be written as

$$PL = L_{I0} - 10 \log_{10} SF, \quad (\text{A3})$$

where L_{I0} is the isotropic free-space path-loss for the impinging wave

$$L_{I0} = 20 \log_{10} \frac{4\pi \rho_i}{\lambda}. \quad (\text{A4})$$

Acknowledgments

The data sets used in this work are available on Figshare at the following URL: <https://figshare.com/s/ff9fb437c38d266d9e25>

References

- Ai, B., Guan, K., He, R., Li, J., Li, G., He, D., et al. (2017). On indoor millimeter wave massive MIMO channels: Measurement and simulation. *IEEE Journal on Selected Areas in Communications*, 35(7), 1678–1690.
- Balanis, C. A. (1989). *Advanced Engineering Electromagnetics*. New York, NY: John Wiley.
- Cheng, C. L., S. Kim, and A. Zajic (2017). Comparison of path loss models for indoor 30 GHz, 140 GHz, and 300 GHz channels, in *Proc. of 11th European Conference on Antennas and Propagation (EuCAP), Paris, France*, pp. 716–720, doi: <https://doi.org/10.23919/EuCAP.2017.7928124>.
- de Jong, Y. L. C., & Herben, M. H. A. J. (2004). A tree-scattering model for improved propagation prediction in urban microcells. *IEEE Transactions on Vehicular Technology*, 53(2), 503–513.
- Degli-Esposti, V., Fuschini, F., & Vitucci, E. M. (2009). A fast model for distributed scattering from buildings, in *Proc. of 3rd European Conference on Antennas and Propagation (EuCAP), Berlin, Germany* (pp. 1–5).
- Degli-Esposti, V., Fuschini, F., Vitucci, E. M., & Falciaesca, G. (2007). Measurement and modelling of scattering from buildings. *IEEE Transactions on Antennas and Propagation*, 55(1), 143–153. <https://doi.org/10.1109/TAP.2006.888422>
- Degli-Esposti, V., Guiducci, D., de Marsi, A., Azzi, P., & Fuschini, F. (2004). An advanced field prediction model including diffuse scattering. *IEEE Transactions on Antennas and Propagation*, 52(7), 1717–1728. <https://doi.org/10.1109/TAP.2004.831299>
- Epstein, J., & Peterson, D. W. (1953). An experimental study of wave propagation at 850 MC. *Proceedings of the IRE*, 41(5), 595–611.
- ESRI Company (1998). Esri shapefile technical description—an esri white paper — july.
- EU law and publications, Bruxelles (2016). Com/2016/0588, accessed 18 July 2018.
- Federal Communications Commission (Washington D.C.) (2018). The fcc's 5g fast plan, accessed 29 April 2019.

- Fuschini, F., El-Sallabi, H., Degli-Esposti, V., Vuokko, L., Guiducci, D., & Vainikainen, P. (2008). Analysis of multipath propagation in urban environment through multidimensional measurements and advanced ray tracing simulation. *IEEE Transactions on Antennas and Propagation*, 56(3), 848–857. <https://doi.org/10.1109/TAP.2008.916893>
- Fuschini, F., Häfner, S., Zoli, M., Müller, R., Vitucci, E. M., Dupleich, D., et al. (2016). Item level characterization of mm-wave indoor propagation. *EURASIP Journal on Wireless Communications and Networking*, 2016(1), 1–12.
- Fuschini, F., Häfner, S., Zoli, M., Müller, R., Vitucci, E. M., Dupleich, D., et al. (2017). Analysis of in-room mm-wave propagation: Directional channel measurements and ray tracing simulations. *Journal of Infrared, Millimeter, and Terahertz Waves*, 38(6), 727–744.
- Fuschini, F., Vitucci, E. M., Barbiroli, M., Falciaeseca, G., & Degli-Esposti, V. (2015). Ray tracing propagation modeling for future small-cell and indoor applications: a review of current techniques. *Radio Science*, 50, 469–485.
- Goldhirsh, J., & Vogel, W. J. (1998). Handbook of propagation effects for vehicular and personal mobile satellite systems. *NASA Reference Publication*, 1274, 40–67.
- Huang, F., Tian, L., Zheng, Y., & Zhang, J. (2016). Propagation characteristics of indoor radio channel from 3.5 GHz to 28 GHz, in *Proc. of IEEE 84th Vehicular Technology Conference (VTC-Fall)*, Montreal, QC, Canada (pp. 1–5). <https://doi.org/10.1109/VTCTFall.2016.7881180>.
- Hur, S., Cho, Y. J., Kim, T., Park, J., Molisch, A. F., Haneda, K., & Peter, M. (2015). Wideband spatial channel model in an urban cellular environments at 28 GHz, in *Proc. of 9th European Conference on Antennas and Propagation (EuCAP)*, Lisbon, Portugal, pp. 1–5.
- Inomata, M., Imai, T., Kitao, K., Okumura, Y., Sasaki, M., & Takatori, Y. (2017). Prediction accuracy of hybrid method based on ray-tracing and effective roughness model in indoor environment for millimeter waves, in *Proc. of IEEE Conference on Antenna Measurements and Applications (CAMA)*, Tsukuba, Japan, pp. 44–46, doi: <https://doi.org/10.1109/CAMA.2017.8273471>.
- Inomata, M., Sasaki, M., Nakamura, M., & Takatori, Y. (2017). Diffuse scattering prediction for 26 GHz band in indoor office environments, in *Proc. of International Symposium on Antennas and Propagation (ISAP)*, Phuket, Thailand, pp. 1–2, doi: <https://doi.org/10.1109/ISANP.2017.8228808>.
- ITU-R (2013). *Recommendation P. 526-13: Propagation by Diffraction*.
- ITU-R (2016). *Recommendation P. 833-9: Attenuation in vegetation*.
- Karstensen, A., Fan, W., Carton, I., & Pedersen, G. F. (2016). Comparison of ray tracing simulations and channel measurements at mmWave bands for indoor scenarios, in *Proc. of 10th European Conference on Antennas and Propagation (EuCAP)*, Davos, Switzerland (pp. 1–5). <https://doi.org/10.1109/EuCAP.2016.7481361>
- Kouyoumjian, R. G., & Pathak, P. H. (1974). A uniform geometrical theory of diffraction for an edge in a perfectly conducting surface. *Proceedings of the IEEE*, 62(11), 1448–1461. <https://doi.org/10.1109/PROC.1974.9651>
- Leonor, N. R., Caldeirinha, R. F. S., Fernandes, T. R., Ferreira, D., & Sánchez, M. G. (2014). A 2D ray-tracing based model for micro- and millimeter-wave propagation through vegetation. *IEEE Transactions on Antennas and Propagation*, 62(12), 6443–6453. <https://doi.org/10.1109/TAP.2014.2362124>
- Mani, F., & Oestges, C. (2011). Ray-tracing evaluation of diffuse scattering in an outdoor scenario, in *Proc. of 5th European Conference on Antennas and Propagation (EuCAP)*, Rome, Italy (pp. 1–5).
- Mani, F., Vitucci, E. M., Barbiroli, M., Fuschini, F., Degli-Esposti, V., Gan, M., et al. (2018). 26 GHz ray-tracing pathloss prediction in outdoor scenario in presence of vegetation, in *Proc. of the 12th European Conference on Antennas and Propagation (EuCAP)*, London, UK.
- Nielsen, J. Ø., & Pedersen, G. F. (2016). Dual-polarized indoor propagation at 26 GHz, in *Proc. of IEEE 27th Annual International Symposium on Personal, Indoor, and Mobile Radio Communications (PIMRC)*, Valencia, Spain (pp. 1–6). <https://doi.org/10.1109/PIMRC.2016.7794751>.
- Park, J. J., Liang, J., Lee, J., Kwon, H. K., Kim, M. D., & Park, B. (2016). Millimeter-wave channel model parameters for urban microcellular environment based on 28 and 38 GHz measurements, in *Proc. of IEEE 27th Annual International Symposium on Personal, Indoor, and Mobile Radio Communications (PIMRC)*, Valencia, Spain (pp. 1–5). <https://doi.org/10.1109/PIMRC.2016.7794731>.
- Radio Spectrum Policy Group (Brussels, 09 November 2016), “RSPG 16-032, Opinion on spectrum related aspects for next-generation wireless systems (5G)”.
- Rappaport, T. S., MacCartney, G. R., Samimi, M. K., & Sun, S. (2015). Wideband millimeter-wave propagation measurements and channel models for future wireless communication system design. *IEEE Transactions on Communications*, 63(9), 3029–3056. <https://doi.org/10.1109/TCOMM.2015.2434384>
- Rappaport, T. S., MacCartney, G. R., Sun, S., Yan, H., & Deng, S. (2017). Small-scale, local area, and transitional millimeter wave propagation for 5G communications. *IEEE Transactions on Antennas and Propagation*, 65(12), 6474–6490. <https://doi.org/10.1109/TAP.2017.2734159>
- Rappaport, T. S., Sun, S., Mayzus, R., Zhao, H., Azar, Y., Wang, K., et al. (2013). Millimeter wave mobile communications for 5G cellular: It will work! *IEEE Access*, 1, 335–349.
- Rappaport, T. S., Xing, Y., MacCartney, G. R., Molisch, A. F., Mellios, E., & Zhang, J. (2017). Overview of millimeter wave communications for fifth-generation (5G) wireless networks - with a focus on propagation models. *IEEE Transactions on Antennas and Propagation*, 65(12), 6213–6230.
- Salous, S., Degli-Esposti, V., Fuschini, F., Thomä, R. S., Müller, R., Dupleich, D., et al. (2016). Millimeter-wave propagation: Characterization and modeling toward fifth-generation systems. [wireless corner]. *IEEE Antennas and Propagation Magazine*, 58(6), 115–127. <https://doi.org/10.1109/MAP.2016.2609815>
- Solomitckii, D., Li, Q. C., Balercia, T., da Silva, C. R. C. M., Talwar, S., Andreev, S., & Koucheryavy, Y. (2016). Characterizing the impact of diffuse scattering in urban millimeter-wave deployments. *IEEE Wireless Communications Letters*, 5(4), 432–435. <https://doi.org/10.1109/LWC.2016.2580669>
- Sun, S., Rappaport, T. S., Shafi, M., Tang, P., Zhang, J., & Smith, P. J. (2018). Propagation models and performance evaluation for 5G millimeter-wave bands. *IEEE Transactions on Vehicular Technology*, 67(9), 8422–8439. <https://doi.org/10.1109/TVT.2018.2848208>
- Vitucci, E. M., Degli-Esposti, V., Fuschini, F., Lu, J. S., Barbiroli, M., Wu, J. N., et al. (2015). Ray tracing RF field prediction: an unforgiving validation. *International Journal of Antennas and Propagation*, 2015.
- Vitucci, E. M., Fuschini, F., Barbiroli, M., Zoli, M., & Degli-Esposti, V. (2018). A study on the performance of Over-Roof-Top propagation models in dense urban environment, in *Proc. of 12th European Conference on Antennas and Propagation (EuCAP)*, London, UK (pp. 1–4).
- Weiler, R. J., Peter, M., Keusgen, W., Sakaguchi, K., & Undi, F. (2016). Environment induced shadowing of urban millimeter-wave access links. *IEEE Wireless Communications Letters*, 5(4), 440–443. <https://doi.org/10.1109/LWC.2016.2581820>
- Weissberger, M. A. (1982). An initial critical summary of models for predicting the attenuation of radio waves by trees, (Tech. Rep.), Electromagnetic Compatibility Analysis Center Annapolis MD.

- World Radiocommunication Conference (Geneve (CH), 2-27 November 2015). Resolution 238, Studies on frequency-related matters for international mobile telecommunications identification including possible additional allocations to the mobile services on a primary basis in portion(s) of the frequency range between 24.25 and 86 GHz for the future development of international mobile telecommunications for 2020 and beyond, (Tech. Rep.), WRC-15.
- Zhong, Z., Li, C., Zhao, J., & Zhang, X. (2017). Height-dependent path loss model and large-scale characteristics analysis of 28 GHz and 38.6 GHz in urban micro scenarios, in *2017 11th European Conference on Antennas and Propagation (EUCAP)*, pp. 1818–1822, doi: <https://doi.org/10.23919/EuCAP.2017.7928640>.